Magnetoelastic and magnetoelectric couplings across the antiferromagnetic transition in multiferroic BiFeO 3

Mariusz Lejman, Charles Paillard, Vincent Juvé, Gwenäelle G. Vaudel, Nicolas Guiblin, Laurent Bellaiche, Michel Viret, Vitali Goussev, Brahim Dkhil, Pascal Ruello

On the magnetoelastic and magnetoelectric couplings across the antiferromagnetic transition in multiferroic $BiFeO_3$

Mariusz Lejman[1], Charles Paillard[2], Vincent Juvé [1], Gwenaelle Vaudel[1], Nicolas Guiblin[3], Laurent Bellaiche [2], Michel Viret [4], Vitalyi E. Gusev[5], Brahim Dkhil [3] and Pascal Ruello[1*]

[1] *Institut des Molécules et Matériaux du Mans, UMR 6283 CNRS, Le Mans Université, 72085 Le Mans, France*

[2] *Department of Physics and Institute for Nanosciences and Engineering, University of Arkansas, Fayetteville, United States.*

[3] *Laboratoire Structures, Propriétés et Modélisation des Solides, CentraleSupélec, UMR CNRS 8580, Université Paris-Saclay, 91190 Gif-sur-Yvette, France*

[4] *SPEC UMR CEA/CNRS, L'Orme les Merisiers, France*

[5] *Laboratoire d'Acoustique de l'Université du Mans, UMR CNRS 6613, Le Mans Université, 72085 Le Mans, France*

Clear anomalies in the lattice thermal expansion (deviation from linear variation) and elastic properties (softening of the sound velocity) at the antiferromagnetic-to-paramagnetic transition are observed in the prototypical multiferroic $BiFeO_3$ using a combination of picosecond acoustic pump-probe and high-temperature X-ray diffraction experiments. Similar anomalies are also evidenced using second-principles calculations supporting our experimental findings. Those calculations, in addition to a simple Landau-like model we also developed,allow to understand the elastic softening and lattice change at T_N as a result of magnetostriction combined with electrostrictive and magnetoelectric couplings, which renormalize the elastic constants of the high-temperature reference phase when the critical T_N temperature is reached.

PACS numbers: 75.85.+t, 75.80.+q, 75.47.Lx, 02.70.Uu, 77.80.Bh, 72.55.+s, 78.35.+c, 61.10.?i

I. INTRODUCTION

Multiferroic materials in which polarization, deformation and magnetic orders coexist have attracted continuous attention because of their tremendous potential in applications such as memories, spintronic devices, sensors/actuators or electro-optical systems as well as their underlying fascinating physics[1,2]. Among them, the room-temperature multiferroic $BiFeO_3$ (BFO)[2] compound represents a rich playground system to understand the complex coupling mechanisms involving electric polarization, spin arrangement and phonon vibration allowing to manipulate their ferroic orders. Although the electrical control of the ferroelectric polarization and its domain distribution in BFO is nowadays well established[4–7], especially using piezo-force microscopy[3], manipulating the antiferromagnetic G-type order (AFM) which appears below Néel temperature $T_N \approx 650$ K, has revealed to be far more difficult, owing to the impossibility of a direct manipulation using magnetic fields. The existence of a magneto-electric (ME) effect, allowing the control of spins with electric fields, may just provide the long-sought route to control the AFM order. However, this ME effect remains weak because of Dzyaloshinskii-Moriya interactions known to be responsible for the non-collinear cycloidal modulation with 62 nm period[15,16] which superimposes to the AFM order.

It is worth mentioning that in addition to electrical and magnetic stimuli, multiferroic properties can be most efficiently tuned using mechanical means. For instance, the ferroelectric polarization can be adjusted by using epitaxial strain or mechanical pressure[8–14]. Similarly, the magnetic order can be also controlled with strain fields through the magneto-elastic coupling. As a result, the energy spectrum of thermally induced magnons (magnetic excitations) in BFO can be drastically modified with engineered static strain in thin films[17,19] or by pressure in bulk[18]. Thus, both the magneto-elastic and magneto-electric couplings impact the magnetic arrangement in BFO, as recently shown in a neutron diffraction study[20].

Actually, the interplay between electric dipoles, magnetic orders and lattice dynamics is complex as further highlighted in a series of recent works. For example, thermal investigation of the phonon density of states (DOS) using neutron scattering revealed a coupling with magnons[21], and a softening of transverse acoustic branches in the vicinity of T_N combined with a phonon peak broadening was as well observed near the AFM transition[22]. This coupling between magnetism and strain in BFO is further confirmed with various techniques such as Raman scattering experiments[23,24], or pulse echo method to evaluate the temperature dependence of the longitudinal elastic modulus [25]. This latter work showed a step-like form softening of the elastic constant ($\sim 0.7\%$) at the Néel transition. Yet, a theoretical work rather suggests a more monotonous change of the sound velocity in the vicinity of the Néel temperature without such softening[26].

Despite this body of works, the mechanisms across the magnetic Néel temperature transition and the role of the various coupling interactions involved in BFO re-

*Electronic address: pascal.ruello@univ-lemans.fr

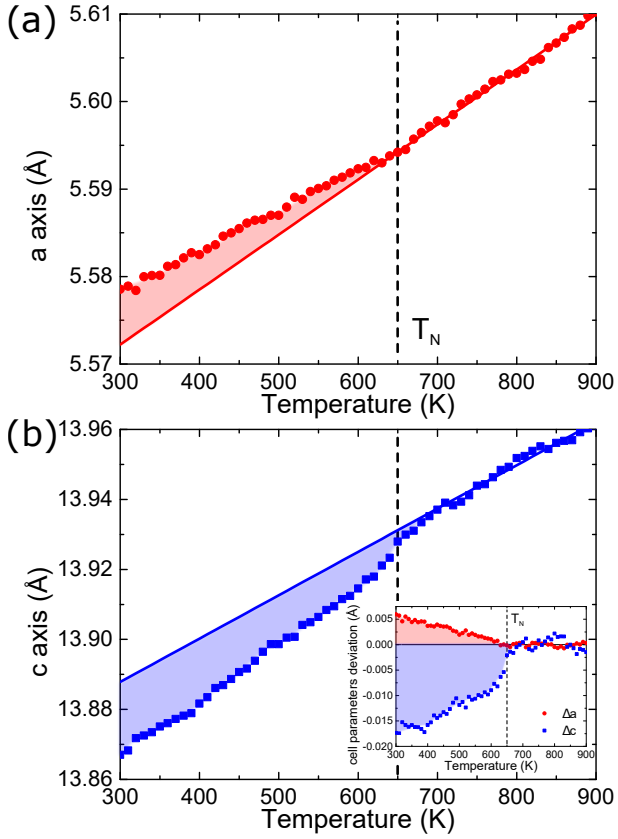

Figure 1: (color online) (a-b) Temperature dependence of the a (top panel) and c (bottom panel) lattice constants of the conventional hexagonal cell. Inset: difference of the unit cell parameters a and c arising below Néel temperature (vertical lines) from the deviation of the linear variation of the thermal expansion.

main elusive. Here, using high-resolution X-ray diffraction (XRD) and picosecond acoustics pump-probe technique combined with second-principles calculations and Landau-based phenomenological approach, we attempt to unravel those mechanisms that couple the AFM order to the lattice dynamics by providing a global experimental and theoretical study of the lattice behavior through the Néel transition. We observe *(i)* a significant and anisotropic change of the thermal expansion coefficients below T_N; and *(ii)* clear softening of the sound velocity of coherent transverse (TA) and longitudinal (LA) acoustic phonons above around 600K and 700K respectively, along with a characteristic kink in the vicinity of the Néel temperature T_N for the TA mode (650-700K). As a matter of fact, significant effects on the lattice of BFO are revealed across the magnetic Néel temperature transition and discussed in the framework of magneto-electric and magneto-elastic couplings. Moreover, the existence of magneto-elastic changes at the GHz range open promising perspectives for the ultra-fast control of AFM (or magnetic) state by strain in future spintronic devices.

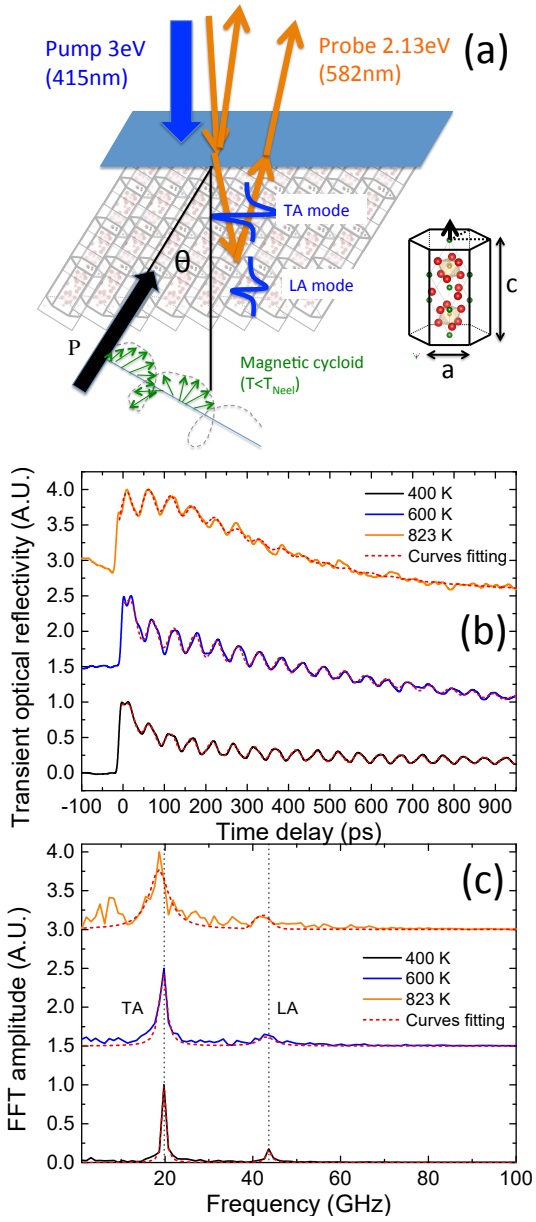

Figure 2: (color online) (a) sketch of the pump-probe experiment conducted with a disoriented BFO grain permitting to emit both LA and TA coherent acoustic phonons[27,29]. (b) Temperature dependence of the time resolved optical reflectivity in $BiFeO_3$ for three selected temperatures. Note that the Néel temperature is about 650K. (c) corresponding Fast Fourier Transform (FFT) of the Brillouin components (TA and LA modes).

II. METHODS

The sample under investigation is a polycrystalline BFO that was already described in previous works[27,28]. The evolution of the $(104)_h$ and $(110)_h$ Bragg diffraction

peaks (in the hexagonal conventional cell) with temperature ranging between 300K and 900 K (precision better than 1 K) was monitored using a high-resolution 2-axis diffractometer equipped with a rotating anode generator of 18 kW (Rigaku), with a Bragg-Brentano geometry and a 50 cm focalisation circle allowing an accuracy as high as 0.0002 Å in 2θ. The unit cell parameters a and c (the latter being along to the polar axis) in the hexagonal setting were then extracted (Fig. 1).

Coherent acoustic phonon dynamics were investigated with a pump-probe set-up developed for high temperature environment. Experiments were conducted on a specific grain of the polycrystalline sample, knowing each grain acts as a single crystal as detailed in Ref.[27]. The orientation of the polar axis with respect to the flat surface of the sample is roughly $\theta \sim 40°$[27]. The BFO grain was photo-excited with above band-gap optical transition (2.6 eV is the bandgap of BFO[30,31]) using a pump beam with 3 eV photon energy having a characteristic penetration of around 50 nm[30,31]). The pump beam impinges on the sample surface with normal incidence, hence making a 40° angle with respect to the polar axis of the grain as shown in Fig. 2a. This pump beam generates LA and TA modes, as discussed in previous papers[27–29]. The photo-generated coherent acoustic waves are then detected using a probe beam with an energy of 2.13 eV well below the bandgap energy and with a normal incidence (the probe beam is inclined in Fig. 2a for clarity). The penetration depth of the probe beam (> 1 μm[30,31]) allows to probe elasticity deep beneath the surface of the sample. Measurements were conducted in air. Heating and cooling cycles were performed to check for reproducibility of the results and stability of the sample. The highest temperature reached was 873 K *i.e.* about 220 K above Néel temperature.

In addition, Metropolis Monte Carlo simulations based on the effective Hamiltonian method described in Refs.[34–37] were carried out in order to gain microscopic understanding of the relevant coupling responsible for the elastic anomalies observed. In essence, this method consists in considering only a few relevant degrees of freedom per 5-atom perovskite cell, here the polarization, the magnetization vector, the tilt of the oxygen octahedra, an inhomogeneous local strain, and a homogeneous strain tensor η_i. A $12 \times 12 \times 12$ supercell of BFO, representing 8640 atoms, was considered. It was cooled down from 1500 K to 5 K under an applied electric field of magnitude $\sqrt{3} \times 10^9$ V.m^{-1} applied along the [111] pseudo-cubic direction to ensure that the low temperature phase is the monodomain $R3c$ ferroelectric ground state. Note that a G-type AFM order is obtained, and no cycloid order is considered in those calculations. 4×10^4 MC sweeps were used during the field cooling procedure. Then, starting from the obtained low temperature field-cooled configuration, the field was removed and the supercell relaxed, starting at the temperature of 5 K and subsequently heating up. During this zero field heating phase, we used 10^6 MC sweeps at each temperature. The various statistical averages used to extract relevant thermodynamic quantities were performed using the last 8×10^5 MC sweeps. The thermal evolution of the relevant degrees of freedom (soft mode, tilt and antiferromagnetic moment) are depicted in the Supplementary Figure 2 of the Note II of the Supplementary Material and show a Néel temperature of about 730 K[38] .

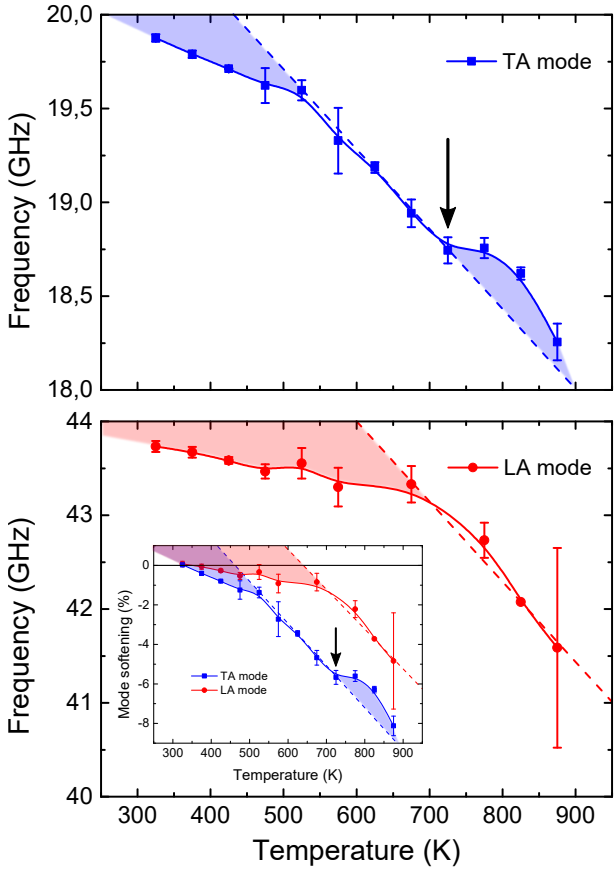

Figure 3: (color online) Temperature dependence of the Brillouin frequencies of the (a) TA and (b) LA modes. The inset in (b) shows the temperature evolution of normalized Brillouin frequencies.

III. RESULTS

Figures 1(a,b) show the thermal evolution of the hexagonal lattice constants a and c. Both unit cell parameters exhibit linear variation in the high-temperature region ($900\ K > T > T_N$). Below the Néel temperature, there is a significant deviation for both lattice constants from the linear variation observed at high temperature, with a contraction of the polar axis c and a change of the thermal expansion slope. This can be more clearly observed once the high-temperature trend is subtracted from the data, as shown in the inset of Fig. 1b. The contraction of the polar axis length below T_N was previously observed in neutron diffraction experiments and attributed to the

magnetostrictive-magnetoelectric coupling caused by the onset of the AFM order[20]. In contrast, the lattice parameter a exhibits a significant elongation (Fig. 1a) below T_N along with a modification of the thermal expansion. This trend is also in agreement with Ref.[20]. The overall volume of the hexagonal unit cell is decreased in the AFM phase below T_N with respect to the extrapolated volume from the high-temperature paramagnetic phase. This result is shown in Supplementary Figure 1 of Ref.[38,39].

Interestingly, the kink observed at T_N in the lattice constants, which are essentially static/time-averaged properties, are concomitant to anomalies observed in the lattice dynamics, as shown in the following. The typical transient optical reflectivity signal (Fig. 2(b)) is composed of a sharp variation when the material is excited by the pump laser followed by a decay in time due to the electronic relaxation. Oscillations are superimposed on this baseline, as previously characterized[27,29]. These oscillations, called Brillouin oscillations, are the results of the time-dependence of optical interferences of the probe beams reflected at the free surface and scattered by the moving acoustic pulses (LA and TA pulses). In other words, due to momentum conservation during the interaction between the probe light wave and the propagating acoustic front (for incident probe beam normal to the surface), only the acoustic phonon component with the Brillouin frequency (f_B) is detected[27,32], accordingly to:

$$f_B = \frac{2nv_s}{\lambda} \tag{1}$$

where λ, n and v_S are the probe wavelength in vacuum, the refractive index of BFO at the wavelength λ and the sound velocity in BFO (of either LA or TA waves), respectively. While BFO is birefringent[28], the effect is limited in the considered orientation and only a mean refractive index was used in the present study. The Brillouin differential reflectivity signal $dR_B(t)$ can be cast in the general form[33]:

$$dR_B(t) \propto sin(2\pi f_B t + \phi) e^{-\beta(T)\times t} e^{-\alpha(T)\times v_s(T) t} \tag{2}$$

where ϕ is the phase of the oscillatory signal and has both a contribution from the phonon field and from the optical detection process[32]. $\beta(T)$ is the intrinsic anharmonic phonon term which governs the phonon damping. The partial penetration of the probe beam can also give rise to a damped signal as soon as the acoustic phonons leave the region of probe penetration. This contribution is described by the term $\alpha(T)v_s(T)$ where α is the optical absorption coefficient at the probe photon energy and v_s is the sound velocity (LA or TA). Based on this formula and applying Fast Fourier Transform (FFT) (shown in Fig. 2(c)) or time-domain fitting, the frequencies of the TA and LA modes are extracted, as well as their damping time. The temperature evolution of the TA and LA frequencies is shown in Figs. 3(a,b). It is clear that the Brillouin frequencies associated with both LA and TA modes do not have a linear dependence with temperature (see inset of Fig. 3b). The TA wave shows a complex temperature behavior. It seems that the Brillouin frequency slightly softens in the vicinity of Néel transition ($710 - 850$ K) with respect to the high-temperature linear trend observed above 800 K, as shown by the arrow in Fig. 3a. Below T_N and more specifically below 710 K, the evolution of the TA Brillouin frequency can be described using two quasi-linear regimes with different slopes, the first occurring between 710 K and 570 K, and the second one below 570 K. The Brillouin frequency is connected to the speed of sound through Eq. (1), and the speed of sound is related to the elastic constant C as $v_s \propto \sqrt{\frac{C}{\rho}}$ with ρ being the density of the medium. Hence the observed softening at T_N may be explained by the softening of elastic constants, as for instance also observed by Smirnova *et al.*[25] in the longitudinal elastic constant. Nonetheless, direct comparison is impeded as Smirnova *et al.* used a polycrystalline sample and thus sample an average of different crystallographic orientations (i.e., elastic constants) while here we study an individual grain/crystal. In contrast to the TA signal, no clear softening at T_N is observed in the LA signal, possibly because of the large damping of the LA signal (see Figs. 2(b,c)) which considerably affects the accuracy of the measurement. Nevertheless, the LA wave (see Fig. 3b) clearly displays two linear regimes with different slopes with the change of regime occurring at the Néel temperature.

Note that the anomalies observed at T_N in the Brillouin frequencies of LA and TA modes could also come from anomalies in the optical index according to Eq. (1). However, no significant change in the optical index was observed through the Néel temperature in previous reports[31], and its evolution is thus considered to be linear with temperature. Besides, the global softening of the TA mode ($\sim 9\%$) is twice as large as that of the LA mode ($\sim 4.5\%$), thus indicating that the observed behaviors come from elastic properties anomalies (see inset of in Fig. 3(b)) and not from optical properties anomalies.

We have also analyzed the damping time. Using the estimates of the absorption coefficient $\alpha(T)$ of Ref.[31], and extrapolating up to 900 K, we have extracted the damping term (αv_s term in Eq. (2)) coming from the finite probe light penetration length. We have found that this last term reproduces well the experimental observations, indicating it dominates over the intrinsic phonon damping characteristic time $\frac{1}{\beta(T)}$ in Eq. (2) excluding the possibility to investigate the spin-phonon collision process.

In order to confirm the elastic origin of the anomalies observed in the LA and TA Brillouin frequencies, we used effective Hamiltonian calculations. The static elastic compliance tensor S_{ij} in the pseudocubic axes was computed from the fluctuations of the homogeneous

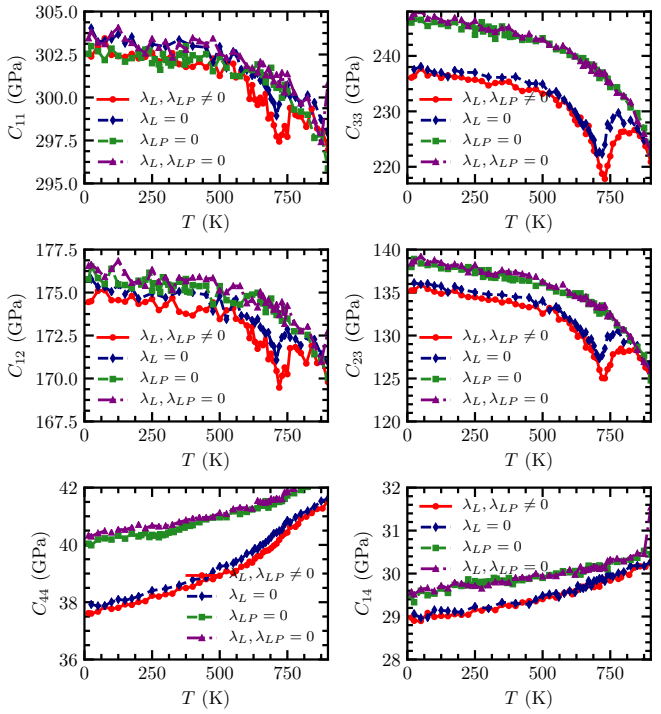

Figure 4: Calculated independent elastic stiffness tensor components C_{ij} in the conventional rhombohedral axes show anomalies at the Néel temperature (red curves). Results with the absence of the magneto- elastic coupling terms in the effective Hamiltonian ($\lambda_L = 0$, blue diamond curve), with the absence of magneto-electric coupling terms ($\lambda_{LP} = 0$, green square curve) and the absence of both ($\lambda_L, \lambda_{LP} = 0$, purple triangle curve) are also shown for comparison.

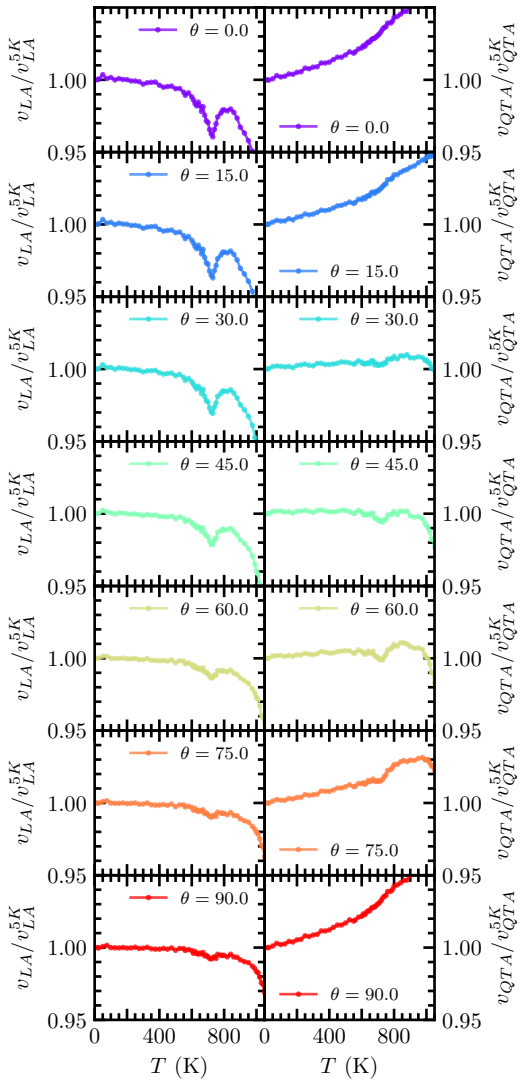

Figure 5: Simulation of the temperature dependence of the LA (left columns) and TA (right columns) sound velocities for variable grain orientation angle θ. The values are normalized to the value obtained at 5K.

strain degrees of freedom,

$$S_{ij} = \frac{\langle V \rangle}{k_B T} \left(\langle \eta_i \eta_j \rangle - \langle \eta_i \rangle \langle \eta_j \rangle \right) \tag{3}$$

with η_i being a pseudocubic strain tensor component (in Voigt notation), k_B being the Boltzmann constant, T the temperature and $\langle V \rangle$ is the mean volume. Secondly, the elastic compliance was transformed into the conventional rhombohedral axes system[40] (corresponding to the pseudocubic directions $[1\bar{1}0]$, $[11\bar{2}]$ and $[111]$ respectively), from which the elastic stiffness tensor C_{ij} was derived using the relations given in Nye[40]. Following this procedure, the elastic constants obtained in the rhombohedral conventional axes are depicted in Fig. (4). The elastic constants obtained at low temperature (5 K) agree well with previous calculations at 0 K from first-principles and related methods[41–43]. The obtained low-temperature evolution for C_{11}, C_{33}, C_{12} and C_{13}, in red circles in Fig. (4)) is rather flat until a significant softening is observed in the temperature range 550 K-850 K. In particular, a softening peak is observed at the computationally predicted Néel temperature of 730 K (see red curves Fig. (4)). Further softening occurs above 850 K, caused by the proximity of the strong first-order ferroelectric-paraelectric phase transition which occurs at about 1100 K. We do not explore this region further as our focus is on the AFM-paramagnetic transition, and its implication on lattice properties. In addition, the transverse elastic constants C_{44} and C_{14} also exhibit a slight (but not as marked as C_{11} or C_{33} for instance) change above the Néel temperature, as the absolute value of their slope increases above T_N.

IV. DISCUSSION

A. Landau model

We have developed a simplified Landau model inspired from Refs.[45–47], purely for a qualitative understanding, which describes *(i)* a second-order phase transition with an antiferromagnetostriction term, *(ii)* a first-order phase ferroelectric transition with an electrostriction term, and includes *(iii)* a bi-quadratic magneto-electric coupling between polarization, P, and antiferromagnetism. The antiferromagnetic order parameter L is coupled to the strain η through a linear-quadratic term $\frac{1}{2}\lambda_L \eta L^2$, and indirectly to it through the magneto-electric coupling term $\lambda_{LP} L^2 P^2$ combined with the electrostrictive term $\lambda_P \eta P^2$. Further details about the model are given in the Ref. [44–47]. The thermodynamic potential Φ with respect to the high-symmetry cubic phase potential Φ_0 can be cast as:

$$\begin{aligned}\Phi - \Phi_0 &= \frac{1}{2}\alpha_L^0 (T - T_N) L^2 + \beta_L L^4 \\ &+ \frac{1}{2}\alpha_P^0 (T - T_0) P^2 + \frac{1}{4}\beta_P P^4 + \frac{1}{6}\gamma_P P^6 \\ &+ \frac{1}{2}\lambda_L \eta L^2 + \frac{1}{2}\lambda_P \eta P^2 + \lambda_{LP} L^2 P^2 + \frac{1}{2} C^0 \eta^2 \quad (4)\end{aligned}$$

with $\alpha_L^0 > 0$, $\beta_L > 0$, $\alpha_P^0 > 0$, $\beta_P < 0$ and $\gamma_P > 0$ constants; C^0 represents the elastic constants in the cubic phase, assumed to be temperature-independent. In other words, we neglect the anharmonic phonon coupling responsible for the temperature dependency of the elastic constants.

Based on the definition of the thermodynamic equilibrium, we can first derive the lattice strain induced in the AFM phase with respect to the strain caused by the ferroelectric order. It can be approximately cast in the form [44–47]

$$\eta = A\,(T_N - T) + B' \left[1 + (1 + D(T_0 - T))^{1/2} \quad ,\right]. \quad (5)$$

where A, B' and D are coefficients.

Secondly a renormalization of the elastic constant C of the material in the antiferromagnetic phase ($T < T_N$) can be derived [44],

$$\begin{aligned}C &= C^0 - \frac{\lambda_P^2}{2\beta_P} \frac{1}{1 + \frac{2\gamma_P}{\beta_P} P^2} - \frac{\lambda_L^2}{2\beta_L} \\ &- \frac{\lambda_{LP}^2}{\beta_P \beta_L} \frac{1}{1 - \frac{\lambda_{LP}^2}{\beta_P \beta_L} + \frac{2\gamma_P}{\beta_P} P^2} \\ &\times \left[\frac{\lambda_P^2}{2\beta_P} \frac{1}{1 + \frac{2\gamma_P}{\beta_P} P^2} + \frac{\lambda_L^2}{2\beta_L} - \frac{\lambda_L \lambda_P}{\lambda_{LP}} \right]. \quad (6)\end{aligned}$$

In Eq. (6), one can clearly separate *(i)* a softening induced by the magnetic transition in red, $-\frac{\lambda_L^2}{2\beta_L}$; *(ii)* a softening at the ferroelectric transition, in blue; and *(iii)* a mixing of the ferroelectric and magnetic softenings caused by the magneto-electric coupling $\lambda_{LP} L^2 P^2$ (in green). We note that the contribution *(i)* was already mentioned in Ref.[25]. The renormalization of the elastic constant is plotted in Supplementary Figures 3-5[44], where we discuss the different contributions (magnetostrictive, electrostrictive, and both the mechanisms at the same time).

We can observe that the experimental strain renormalization of the lattice parameter a (see inset of Fig. 1b) appears to be consistent with the linear term $A\,(T_N - T)$ shown in Eq (5) as if the magnetostrictive term prevails in comparison to the electrostrictive-piezoelectric term (i.e. $A > B'$). In contrast, the renormalization of experimental lattice parameter c (along which the ferroelectric order takes place) does not follow a linear temperature dependence (see inset of Fig. 1b) which may indicate in that case that both the magnetostrictive (A) and electrostrictive-piezoelectric /magnetoelectric-piezoelectric (B') terms contribute, without being possible to provide at this stage a quantitative estimate. It is worth to mention that the tensorial nature of the Landau model can be accounted for and separate expressions for the a (i.e., η_1) and the c axis (i.e., η_3) can be obtained [44], but the qualitative physical ingredients are already included in Eq. (5).

In order to compare the experimental results of elastic properties with effective Hamiltonian calculations, we calculated the velocity of sound for different grain orientations, each of which involves different mixtures of elastic constants because of the inclination of the grain/crystal at an angle θ [48,49]. The determination of the TA and LA sound velocity has been performed with elastic constant computed with the magneto-elastic and magnetoelectric interaction terms ($\lambda_L, \lambda_{LP} \neq 0$), see red curves in Fig. 4. The results, plotted in Fig. 5, show that the LA wave sound velocity should exhibit a clear softening peak at T_N for all grain orientations. This theoretical prediction of the softening at the Néel temperature (dip) would be consistent with the observations of Smirnova *et al.*[25]. In our specific case ($\theta \approx 40°$, close to 45°), this magnetic anomaly (dip of sound velocity) is not observed in Fig. 3b, but the non-linear decrease of the Brillouin frequency with the temperature (Fig. 3b), clearly different from a linear regime expected for a phonon-phonon anharmonic behavior, likely reproduces the envelop of the predicted renormalization of the elastic constant due to the magnetostrictive-magnetoelectric-electrostrictive couplings (Supplementary Figures 4 and 5 in Ref.[44]). The agreement with experiments is much better for the TA waves, since the calculated sound velocity value v_{TA} for $\theta = 45°$ in Fig. 5 predicts a small softening near T_N, which actually is qualitatively consistent with the observed kink in the TA Brillouin frequency in Fig. 3a (see arrow). However, calculations predict an almost temperature-independent TA sound velocity below 575-600 K, while a continuous variation of the TA Brillouin

frequency is observed in Fig. 3a. One should however remember that the effective Hamiltonian does not include the complete set of anharmonic phonon-phonon interactions, and thus the elastic constants of the high temperature cubic phase are nearly temperature independent, whilst they should typically harden at low temperature. As a result, we are missing a global linear baseline variation in the calculated sound velocity which may account for some of the discrepancies between our simulated results and the observed evolution of the Brillouin frequencies of the TA and LA waves.

The physical origin of these elastic anomalies in the vicinity of the Néel temperature is complex since a combination of magnetostrictive, electrostrictive and magnetoelectric effects actually exist. In order to unveil the microscopic origin of the observed elastic softening at the Néel temperature, we carried out three additional calculations.

B. Disabling magneto-elastic coupling

In the first one, denoted $\lambda_L = 0$, and depicted as blue diamond symbols in Fig. (4), we set all coupling terms of the form $G_{ij,l,\alpha\gamma}\eta_l(i)m_{i\alpha}m_{j\gamma}$ ($m_{i\alpha}$ is the α^{th} component of the magnetic moment at site i, and $\eta_l(i)$ the l^{th} component of the strain tensor) to vanish[36]. This effectively precludes any direct/intrinsic magneto-elastic coupling between magnetic moments and strain, which is why we denote it $\lambda_L = 0$, in analogy with the term $\lambda_L \eta L^2$ later described in a simplified Landau model above. Fig. (4) shows that the elastic softening is slightly shifted at lower temperature, which correlates with the slight shift of Néel temperature observed as well [44]. The elastic softening survives, although its depth is reduced by 28% and 38% for C_{11} and C_{33}.

C. Disabling the direct magneto-electric coupling

In the second set of calculations, denoted $\lambda_{LP} = 0$ and depicted as green square in Fig. (4), we set *only* all coupling terms of the form $E_{ij,\alpha\beta\gamma\delta}m_{i,\alpha}m_{j,\beta}u_{i,\gamma}u_{i,\delta}$ to zero[36]. We thus effectively remove the direct magneto-electric interaction that couples magnetic moments with electric dipoles. In a crude approximation, the term $\lambda_{LP}L^2P^2$ that is used in the Landau model above is neglected, hence the notation $\lambda_{LP} = 0$. In this case, we observe the Néel temperature to be shifted down by roughly 350 K! In addition, no elastic softening is observed at the new Néel temperature, highlighting the crucial role of the magneto-electric coupling with the converse piezoelectric effect in the modifications of the elastic properties across T_N.

D. Disabling both the magneto-electric and magneto-elastic couplings

In the latter set of calculations, denoted $\lambda_L, \lambda_{LP} = 0$ and depicted with purple triangles in Fig. (4), we set simultaneously to zero all coupling terms described in the two previous section. The results are not very different from the case $\lambda_{LP} = 0$.

V. CONCLUSION

Using a combination of experimental and theoretical investigations of the complex coupling of polarization, magnetization and deformation in $BiFeO_3$, this work highlights the significant coupling of strain with the AFM order. Indeed, anomalies at the Néel temperature are detected both in experiments, via the evolution of Bragg peaks (static regime) and acoustic waves Brillouin frequencies (dynamic regime), and modeling *via* the temperature evolution of the elastic constants using both second-principles and Laudau-based calculations. Our results indicate a crucial role of the magnetostricive contribution for the lattice parameter a while a combination of magnetostrictive and electrostrictive effects are found to be active on the polar lattice parameter c, as further confirmed by effective Hamiltonian based Monte Carlo simulations. Interestingly, there is a qualitatively good agreement between the experimental observations (especially for the TA waves) and the calculated results in Figs. 3 and 4. The calculations strongly support a crucial role of the magnetoelectric coupling with the converse piezoelectric effect in the renormalization of the elastic constants across T_N, and hence in the anomalies of the sound velocities. Additional picosecond acoustics experiments are now necessary to further explore the complex anisotropic effect our calculations have predicted for various crystal orientations as shown in Fig. 5. Moreover, further pump-probe experiments could be also envisioned with probe wavelength in the near infra-red to increase the probe light penetration in order to extract the damping of acoustic phonons coming from phonon-phonon and phonon-spin collisions. Besides these perspectives, our results demonstrate that the existing coupling between magnetic ordering and strain paves the way for possible coherent control of antiferromagnons with coherent acoustic phonons, in line with the recent ultrafast magneto-acoustic experiments in ferromagnetic materials[50–54].

Acknowledgments. M. L. would like to thank the Ecole Doctorale 3MPL (Matiere Molecules et Materiaux, Pays de la Loire France) for his PhD grant. C. P. and L. B. acknowledge the ARO grant W911NF-16-1-0227. V. J, G. V, V. G and P. R thank Le Mans Acoustique grant "Ferrotransducer project" 2015-2019. G. V, V. J, N. G, B. D, C. P, M. V, V. G and P. R thank the French National Research Agency for support with the project UP-DOWN (N° ANR-18-CE09-0026-04) and

SANTA (N° ANR-18-CE24-0018-03).

[1] K. Wang, J.-M. Liu, and Z. Ren, Adv. Phys. **58**, 321 (2009).
[2] G. Catalan and J.F. Scott, Adv. Mater. **21**, 2463 (2009).
[3] F. Zavalichea, P. Shafer, and R. Ramesh, Appl. Phys. Lett. **87**, 182912 (2005).
[4] H. Béa, B. Dupé, S. Fusil, R. Mattana, E. Jacquet, B. Warot-Fonrose, F. Wilhelm, A. Rogalev, S. Petit, V. Cros, A. Anane, F. Petroff, K. Bouzehouane, G. Geneste, B. Dkhil, S. Lisenkov, I. Ponomareva, L. Bellaiche, M. Bibes, and A. Barthélémy, Phys. Rev. Lett. **102**, 217603 (2009).
[5] R. J. Zeches, M. D. Rossell, J. X. Zhang, A. J. Hatt, Q. He, C.-H. Yang, A. Kumar, C. H. Wang, A. Melville, C. Adamo, G. Sheng, Y.-H. Chu, J. F. Ihlefeld, R. Erni, C. Ederer, V. Gopalan, L. Q. Chen, D. G. Schlom, N. A. Spaldin, L. W. Martin, R. Ramesh, Science **326**, 977 (2009)
[6] C. Beekman W. Siemons T. Z. Ward M. Chi J. Howe M. D. Biegalski N. Balke P. Maksymovych A. K. Farrar J. B. Romero P. Gao X. Q. Pan D. A. Tenne H. M. Christen, Adv. Mater. **25**, 5561 (2013).
[7] A. R. Damodaran C-W. Liang, Q. He, C-Y. Peng, L. Chang, Y-H. Chu, L. W. Martin, Adv. Mater. **23**, 3170 (2011).
[8] I. C. Infante, S. Lisenkov, B. Dupé, M. Bibes, S. Fusil, E. Jacquet, G. Geneste, S. Petit, A. Courtial, J. Juraszek, L. Bellaiche, A. Barthélémy, and B. Dkhil, Phys. Rev. Lett. **105**, 057601 (2010).
[9] I. C. Infante, J. Juraszek, S. Fusil, B. Dupé, P. Gemeiner, O. Dieguez, F. Pailloux, S. Jouen, E. Jacquet, G. Geneste, J. Pacaud, J. Iniguez, L. Bellaiche, A. Barthélémy, B. Dkhil, and M. Bibes, Phys. Rev. Lett **107**, 237601 (2011).
[10] M. Guennou, P. Bouvier, G. S. Chen, B. Dkhil, R. Haumont, G. Garbarino, J. Kreisel, Phys. Rev. B **84**, 174107 (2011).
[11] Y. Yang, I.C. Infante, B. Dkhil, L. Bellaiche, Comptes Rendus Physique, **16**, 193 (2015).
[12] B. Dupé, I. C. Infante, G. Geneste, P.-E. Janolin, M. Bibes, A. Barthélémy, S. Lisenkov, L. Bellaiche, S. Ravy, and B. Dkhil., Phys. Rev. B **81**, 144128 (2010).
[13] B. Dupé, S. Prosandeev, G. Geneste, B. Dkhil, and L. Bellaiche, Phys. Rev. Lett **106**, 237601 (2011).
[14] D. Edwards, N. Browne, K. Holsgrove, A. B. Naden, S. O. Sayedaghaee, B. Xu, S. Prosandeev, D. Wang, D. Mazumdar, M. Duchamp, A. Gupta, S. V. Kalinin, M.A. Arredondo, R. G. P. McQuaid, L. Bellaiche, J. M. Gregg and A. Kumar, Nanoscale **10**, 17629 (2018)
[15] I. Sosnowska, T. P. Neumaier, E. Steichele, J. Phys. C Solid State Phys. **15**, 4835-4846 (1982).
[16] D. Rahmedov, Dawei Wang, Jorge Íñiguez and L. Bellaiche, Physical Review Letters **109**, 037207 (2012).
[17] P. Rovillain, R. de Sousa, Y. Gallais, A. Sacuto, M. A. Méasson, D. Colson, A. Forget, M. Bibes, A. Barthélémy, M. Cazayous, Nat. Mater. **9**, 975-979 (2010).
[18] J. Buhot, C. Toulouse, Y. Gallais, A. Sacuto, R. de Sousa, D. Wang, L. Bellaiche, M. Bibes, A. Barthélémy, A. Forget, D. Colson, M. Cazayous, and M-A. Méasson, Physical Review Letters **115**, 267204 (2015).
[19] D. Sando, A. Agbelele, D. Rahmedov, J. Liu, P. Rovillain, C. Toulouse, I. C. Infante, A. P. Pyatakov, S. Fusil, E. Jacquet, C. Carrétéro, C. Deranlot, S. Lisenkov, D. Wang, J-M. Le Breton, M. Cazayous, A. Sacuto, J. Juraszek, A. K. Zvezdin, L. Bellaiche, B. Dkhil, A. Barthélémy, M. Bibes, Nature Mater. **12**, 641-646 (2013).
[20] S. Lee,M. T. Fernandez-Diaz, H. Kimura, Y. Noda, D. T. Adroja, S. Lee, J. Park, V. Kiryukhin, S.-W. Cheong, M. Mostovoy, and Je-Geun Park, Phys. Rev. B **88**, 060103(R) (2013).
[21] O. Delaire, M. B. Stone, J. Ma, A. Huq, D. Gout, C. Brown, K. F. Wang, and Z. F. Ren, Phys. Rev. B **85**, 064405 (2012).
[22] J. A. Schneeloch, Z. Xu, J. Wen, P. M. Gehring, C. Stock, M. Matsuda, B. Winn, G. Gu, Stephen M. Shapiro, R. J. Birgeneau, T. Ushiyama, Y. Yanagisawa, Y. Tomioka, T. Ito, and G. Xu, Phys. Rev. B **91**, 064301 (2015).
[23] T. Shimizu, T. Era, H. Taniguchi, D. Fu, T. Taniyama, and M. Itoh, Ferroelectrics **403**, 187 (2010).
[24] P. Rovillain, M. Cazayous, Y. Gallais, and A. Sacuto, R. P. S. M. Lobo, D. Lebeugle, D. Colson, Phys. Rev. B. **79**, 180411(R) (2009).
[25] E.P. Smirnova, A. Sotnikov, S. Ktitorov, N. Zaitseva, H. Schmidt, and M. Weihnacht, Eur. Phys. J. B **83**, 39-45 (2011)
[26] X-S. Cao, G-F. Ji, X-F. Jiang, Solid State Communications **245** 55-59 (2016).
[27] M. Lejman, G. Vaudel, I.C. Infante, P. Gemeiner, V. Gusev, B. Dkhil, P. Ruello, *Nature Comm.* **5**, 4301 (2014).
[28] M. Lejman, G. Vaudel, I.C. Infante, I. Chaban, T. Pezeril, M. Edely, G. F. Nataf, M. Guennou, J. Kreisel, V. Gusev, B. Dkhil, P. Ruello, Nature Comm. **7**, 12345 (2016).
[29] P. Ruello, T. Pezeril, S. Avanesyan, G. Vaudel, V. Gusev, I.C. Infante, B. Dkhil, Appl. Phys. Lett. **100**, 212906 (2012).
[30] S. G. Choi,H. T. Yi, S.-W. Cheong, J. N. Hilfiker, R. France, and A. G. Norman Phys. Rev. B **83**, 100101(R) (2011).
[31] V. Zelezny, D. Chvostova, L. Pajasova, I. Vrejoiu, M. Alexe, App. Phys. A **100**, 1217-1220 (2010).
[32] C. Thomsen, H. T. Grahn, H. J. Maris, and J. Tauc, Phys. Rev. B **34**, 4129 (1986).
[33] V. Gusev, P. Ruello, App. Phys. Rev., **5**, 031101 (2018)
[34] I. A. Kornev, L. Bellaiche, P.-E. Janolin, B. Dkhil, E. Suard, *Phys. Rev. Lett.* **97**, 157601 (2006).
[35] I. A. Kornev, S. Lisenkov, R. Haumont, B. Dkhil, L. Bellaiche, *Phys. Rev. Lett.* **99**, 227602 (2007).
[36] D. Albrecht, S. Lisenkov, W. Ren, D. Rahmedov, I. A. Kornev, L. Bellaiche, *Phys. Rev. B* **81**, 140401 (2010).
[37] S. Prosandeev, D. Wang, W. Ren, J. Íñiguez, L. Bellaiche, *Adv. Func. Mater.* **23**, 234 (2013).
[38] The supplementary informations are available online.
[39] In the Note I of the SM[38] we show in the Supplementary Figure 1 the contraction of the lattice unit cell volume at the Néel transition.
[40] J. F. Nye, *Physical Properties of Crystals*, Oxford University Press (1985).
[41] P. Marton, A. Klíč, M. Paściak, and J. Hlinka, *Phys. Rev.*

B **96**, 174110 (2017).
[42] S. L. Shang, G. Sheng, Y. Wang, L. Q. Chen, and Z. K. Liu, *Phys. Rev. B* **80**, 052102 (2009).
[43] E. Borissenko, M. Goffinet, A. Bosak, P. Rovillain, M. Cazayous, D. Colson, Ph. Ghosez, M. Krisch, *J. Phys.: Condens. Matter* **25**, 102201 (2013).
[44] The Landau model that is developed is described in the Note III of the Supplementary Informations[38]. This model is partially based on previous work cited in Refs.[45? ,46]
[45] J. C. Slonczewski, H. Thomas, *Phys. Rev. B* **1**, 3599 (1970).
[46] M. A. Carpenter, E. K. H. Salje, Eur. J. Mineral **10**, 683 (1998).
[47] E. K. H. Salje, M. A. Carpenter, *J. Phys.: Condens. Matter* **23**, 462202 (2011).
[48] In the Supplementary Note IV of the Supplementary Informations[38], we provide the detailed expressions of the the longitudinal (v_{LA}) and transverse (v_{TA}) sound velocity as a function of the $BiFeO_3$ grain orientation θ and of the elastic constants C_{ij}.
[49] W. P. Mason, *Physical Acoustics*, Academic Press (1976).
[50] J-W. Kim, M. Vomir, J-Y. Bigot, Phys. Rev. Lett. 109, 166601 (2012).
[51] A.V. Scherbakov, A.S. Salasyuk, A.V. Akimov, X. Liu, M. Bombeck, C. Brüggemann, D.R. Yakovlev, V.F. Sapega, J.K. Furdyna, M. Bayer, Phys. Rev. Lett. **105**(11), 117204 (2010).
[52] O. Kovalenko, T. Pezeril, V.V. Temnov, Phys. Rev. Lett. 110 (26), 266602 (2013).
[53] L. Thevenard, C. Gourdon, J-Y. Prieur, H. Jürgen Von Bardeleben, S. Vincent, L. Becerra, L. Largeau, J-Y. Duquesne, Phys. Rev. B **90**(9), 094401 (2014).
[54] J. Janusonis, T. Jansma, C.L. Chang, Q. Liu, A. Gatilova, A.M. Lomonosov, V. Shalagatskyi, T. Pezeril, V.V. Temnov, R.I. Tobey, Sci. Rep. **6**, 29143 (2016)